Materials Advances

ROYAL SOCIETY OF CHEMISTRY

PAPER

View Article Online
View Journal | View Issue

Cite this: *Mater. Adv.*, 2025, 6, 3331

An AIE-active fluorophore based dibenzothiophene-*S,S*-dioxide unit for highly efficient fluorescence imaging and photodynamic therapy†

Liwen Hu,[a] Tianze Hu,[b] Ting Guo *[b] and Chunxiao Wang*[c]

In this work, we introduced an AIE-active small molecule fluorophore (SOTA) based on electron-withdrawing dibenzothiophene-*S,S*-dioxide. Thanks to the robust intramolecular charge-transfer characteristic of SOTA with D–A–D architecture, the water-soluble nanoparticles (SOTA NPs) presented impressive two-photon absorption properties and efficient intersystem crossing. A high two-photon absorption cross-section of 7247 GM upon excitation at 700 nm enabled it to be successfully implemented in vascular imaging of *in vivo* and *ex vivo* tissues. A moderate penetration depth of 295 μm and an extremely high SNR value of 46 were obtained in two-photon fluorescence imaging for bladder vessels. Moreover, with the aid of the T_2 state, the possibility of intersystem crossing from S_1 to T_1 was further elevated, which was conducive to attaining superior reactive oxygen species (ROS) generation yields. Decent ROS generation capability was confirmed by the attenuated absorption of 9,10-anthracenediyl-bis(methylene)dimalonic acid (ABDA) and electron paramagnetic resonance (EPR) experiments for SOTA nanoparticles. A ROS yield of 58.5% was achieved under white light irradiation. The positive photodynamic therapeutic effect on A549 cells has been convincingly demonstrated *in vitro*. The results indicated that SOTA nanoparticles can be used for two-photon fluorescence imaging and photodynamic therapy.

Received 13th February 2025,
Accepted 20th April 2025

DOI: 10.1039/d5ma00134j

rsc.li/materials-advances

Introduction

Thanks to its high sensitivity, excellent selectivity, non-invasiveness, and versatility, fluorescence imaging technology has been experiencing unprecedented development in the fields of disease diagnosis,[1,2] drug delivery,[3,4] and surgical navigation.[5,6] Recently, it has focused on near-infrared windows (NIR-I, 700–900 nm; NIR-II, 900–1700 nm) rather than the visible region (400–700 nm). The adverse effects of light scattering and autofluorescence from biological tissues were minimized, so that the imaging results with an improved signal-to-noise ratio (SNR) and spatial-temporal resolution were captured.[7–9] However, further enhancement of fluorescence brightness and penetration depth of the existing NIR organic dyes was still urgent. Both the molar extinction coefficient (ε) and the fluorescence quantum yield (η) were well-identified as critical factors in modulating the brightness of organic dyes.[10] Nonetheless, optimization of these two parameters failed to materialize simultaneously for typical donor–acceptor (D–A) type organic dyes.[11,12] Current evidence has shown that it was preferable to extend the conjugation length to maximize the molar extinction coefficient (ε),[13] although the intramolecular charge transfer was bound to be intensified, with a reduction in the highest occupied molecular orbital (HOMO) and the lowest unoccupied molecular orbital (LUMO) electron cloud overlapping. Hence, the radiative transition rate decelerated, along with an eventual decrease in the fluorescence quantum yield. An alternative well-established strategy to amplify ε value was to optimize the molecular planarity of organic fluorescence dyes.[14,15] What should be mentioned was that this implicitly allowed for enhanced intermolecular interactions, and boosted π–π packing, bringing about aggregation-caused quenching (ACQ) performance. Consequently, it was an obstacle to their biological applications.

An enormous attempt has been made to address the ACQ problem of organic dyes, and one research hotspot was to

[a] *School of Optoelectronic Engineering, Guangdong Polytechnic Normal University, Guangzhou 510665, P. R. China*
[b] *Institute of Polymer Optoelectronic Materials and Devices, State Key Laboratory of Luminescent Materials and Devices, South China University of Technology, Guangzhou 510640, China. E-mail: mstguo@scut.edu.cn*
[c] *State Key Laboratory of Ophthalmology, Zhongshan Ophthalmic Center, Sun Yat-sen University, 54 S Xianlie Road, Guangzhou 510060, China. E-mail: wangchunxiao@gzzoc.com*

† Electronic supplementary information (ESI) available. See DOI: https://doi.org/10.1039/d5ma00134j

explore AIE fluorophores (AIEgens). These fluorophores were confirmed to be a class of biomedical materials with the foremost potential for practical clinical applications, due to the distinguished merits of bright luminescence in the aggregated state, large Stokes shift, good photostability, as well as high SNR value.[16–19] In addition to the star building block tetraphenylethene (TPE), triphenylamine (TPA) was also prevalent in the construction of AIEgens on account of its TPE-like stereoscopic effect.[20–22] Three phenyl groups dissipated excited-state energy by means of ongoing rotational motion in solution, in contrast, the intramolecular rotation in the aggregated state was limited. Therefore, we intended to design an AIE-active fluorophore by integrating an acceptor group into the TPA donor. The electron-deficient dibenzothiophene-*S*,*S*-dioxide (SO) unit with a rigid and planar skeleton was conducive to boosting high fluorescence quantum yield. More importantly, the sulfur element with non-metal heavy-atom effect could facilitate amplifying spin-orbital coupling and accelerating intersystem crossing (ISC) process of SO-based fluorophores upon photoexcitation.[23,24] This feature endows them with photosensitizing properties to kill cancer cells in photodynamic therapy (PDT).

Due to its non-invasive and high specificity toward malignant tissues, PDT has been categorized as one clinically approved modality for cancer treatment.[25,26] AIEgens have been reported to have better fluorescence and ROS generation after being endocytosed by cells, distinguishing them in fluorescence bioimaging and PDT applications.[27] Therefore, an AIE-active fluorophore, 3,7-bis(4-(diphenylamino) phenyl)-2,8-dioctyldibenzo[*b*,*d*]thiophene 5,5-dioxide (SOTA) was constructed with D–A–D structural design. Then we thoroughly investigated the photophysical properties of SOTA. Interestingly, it displayed two-photon absorbance properties with a high two-photon absorption cross-section up to 7247 GM. Thus, after encapsulating SOTA into nanoparticles, two-photon fluorescent imaging of three tissues (bladder, peritoneum, and liver) was acquired and penetrated up to 360 μm. Moreover, the intensified ICT effect between SO and TPA units rendered AIEgen to achieve HOMO and LUMO isolation and a small singlet–triplet energy gap (ΔE_{ST}), in turn, the ISC process was further enhanced. Hence, SOTA possessed ideal ROS production with a $^1O_2$ yield of 58.5%, slightly better than that of the commercial PS, methylene blue (MB), achieving positive photodynamic treatment efficacy against A549 cells (Scheme 1).

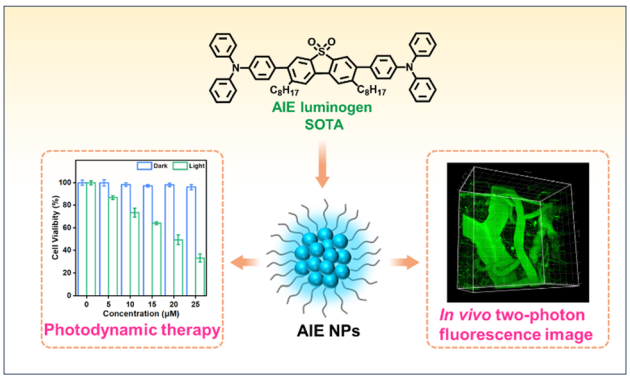

Scheme 1 Schematic illustration of SOTA nanoparticles preparation and their application as a two-photon fluorescence probe and photosensitizer.

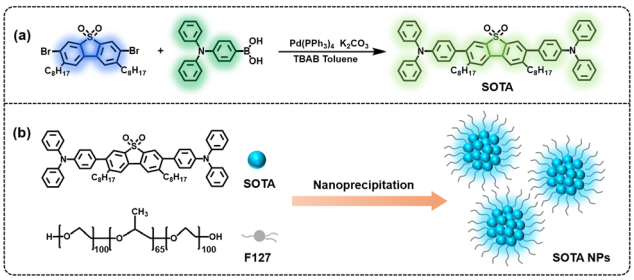

Scheme 2 (a) Synthesis route of AIEgen (SOTA). (b) Preparation of SOTA NPs.

Results and discussion

Preparation and optical properties of SOTA

The targeted compound SOTA was readily synthesized from 3,7-dibromo-2,8-dioctyldibenzo[*b*,*d*]thiophene 5,5-dioxide and (4-(diphenylamine)phenyl)boronic acid in one straightforward step with a satisfactory yield of 85%. The important intermediate SO core was obtained according to the literature reported by our teams.[28] The detailed synthesis route and process were summarized in Scheme 2. The structure of SOTA was well-characterized by NMR and MS analysis (Fig. S1–S3, ESI†). In Fig. S4 (ESI†), the strong signals of 2930 cm^{-1} and 1589 cm^{-1} were assigned to aromatic C–H stretching vibration and aromatic C–N stretching vibration, respectively. Another important signal at 1277 cm^{-1} was associated with the stretching vibration of the sulphone group (O═S═O). This result also validated the structure of SOTA. Based on the cyclic voltammetry measurements, the HOMO/LUMO energy levels of SOTA were estimated to be −5.36/−2.61 eV by the onset of oxidation and reduction curves (Fig. S5, ESI†).

The optical property of SOTA was initially investigated in a dilute THF solution. The intense absorption at 300 nm was attributed to the local π–π* transition of its conjugated skeleton, with the shoulder band at 360 nm resulting from intramolecular charge transfer (ICT) transition from TPA donor to SO acceptor. Additionally, SOTA emitted a sky-blue fluorescence with its peak at 481 nm as well as a large Stokes shift of 121 nm (Fig. 1a). Solvatochromic effect was exhibited for molecules with D–A–D configuration in the form of dependence of the photophysical properties on solvent polarity. Accordingly, UV-visible absorption and photoluminescence (PL) spectra of SOTA were collected in several solvents of different polarities. The absorption spectra of SOTA were essentially invariable with no apparent shift in response to changes in solvent polarity (Fig. S6, ESI†). Brilliant fluorescence emerged at 418 and 438 nm in the low-polarity solvents hexane and toluene (Fig. 1b), exhibiting outstanding fluorescence quantum

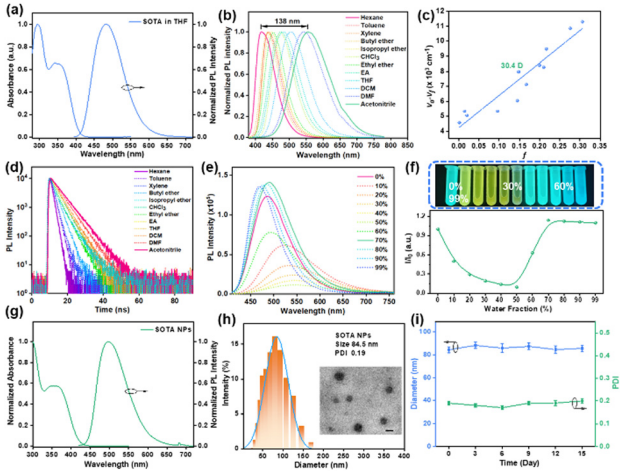

Fig. 1 (a) The absorbance and fluorescent spectra of SOTA in THF solution. (b) The fluorescent spectra of SOTA in different solutions. $CHCl_3$: chloroform; EA: ethyl acetate; THF: tetrahydrofuran; DCM: dichloromethane; DMF: dimethyl formamide. (c) Lippert–Mataga plots in different solvents. (d) Fluorescence lifetimes of SOTA in different solutions. (e) The fluorescent spectra of SOTA (5×10^{-5} M) in the THF/water mixed solvents with various f_w values. (f) Relative peak fluorescent intensity of SOTA in the THF/water mixed solvents with various f_w values as referenced to the fluorescent intensity of SOTA in THF solution (I/I_0); the photos are SOTA in the THF/water solvents with the f_w of 0% and 99%, respectively, taken under 365 nm UV light. (g) The absorbance and fluorescent spectra of SOTA NPs. (h) Particle size distribution of SOTA NPs (the inset is the TEM image of SOTA NPs, scale bar is 100 nm). (i) Storage stability of SOTA NPs.

yields (QYs) of 70.9% and 73%, respectively (Table 1). In the high-polarity acetonitrile solvent, the green fluorescence peaked at 555 nm with a redshift of 136 nm, displaying a substantial reduction in fluorescence intensity and fluorescence quantum yield. This was dependent on the fact that CT-like molecules showed differentiated fluorescence responses in polar and nonpolar solvents. A combination of strong intermolecular interactions with polar solvents and restricted vibrational modes in the excited state accounted for the diminished fluorescence. We additionally utilized the Lippert–Mataga equation to quantify the ICT intensity of SOTA. In Fig. 1c, the excited state dipole moment was 30.4 D, typical for charge transfer molecules. It emitted bright fluorescence with high QY varying from 42% to 85%, attributable to the existence of the SO unit. Concurrently, its fluorescence lifetimes were short with 1.5–6.0 ns in a solution polarity-dependent manner (Table S1, ESI†). A prolonged lifetime of SOTA was observed in the more polar solvents. The fluorescent quantum yield of SOTA in the pure film state was determined to be 85.3%, higher than that of SOTA in solutions as expected (Table 1).

Table 1 Detailed photophysical properties data of AIEgen (SOTA) in solvents with different polarities

SOTA	$f(\varepsilon,n)^a$	$\lambda_{abs}{}^b$ (nm)	$\lambda_{PL}{}^c$ (nm)	V_a–$V_f{}^d$ (cm^{-1})	Φ^e (%)	τ^f (ns)
Hexane	0.0012	351	418	4566.6	70.4	1.51
Toluene	0.014	355	438	5338.0	73.0	1.85
Xylene	0.02	360	440	5050.5	70.5	1.92
Butyl ether	0.096	353	435	5340.1	74.2	2.55
Isopropyl ether	0.145	352	447	6037.7	72.8	3.14
Chloroform	0.147	344	474	7972.7	78.3	3.91
Ethyl ether	0.167	343	454	7128.1	81.7	3.19
Ethyl acetate	0.2	340	476	8403.4	82.7	4.27
Tetrahydrofuran	0.21	344	481	8279.8	83.9	3.92
Dichloromethane	0.217	341	504	9484.2	84.5	4.28
Dimethyl formamide	0.276	342	544	10857.4	53.4	4.91
Acetonitrile	0.306	341	555	11307.5	42.3	5.56

[a] The orientation polarizability of solvents. [b] Absorption of ICT band. [c] Emission maxima. [d] Stokes shift value. [e] Fluorescence quantum yield. [f] Fluorescence lifetime detected at the maximum fluorescence wavelengths.

The AIE behavior of SOTA was authenticated by comparing its FL spectra in the traditional THF/water mixed solvents with water contents (f_w) of 0–90% and 99% (Fig. 1e). When f_w value dropped below 60%, the fluorescence intensity of SOTA was negatively correlated with the water content, and a decrease of fluorescence intensity by 80% was observed. The solubility of SOTA was ruled out as originating from the presence of *n*-octyl alkyl chains in SOTA. A continued increase in the f_w value up to 99% was associated with a sudden increase in the fluorescence intensity of SOTA. Additionally, a blue-shifted tendency was recorded in the wavelength of PL spectra (Fig. S7, ESI†). The most intense fluorescence of SOTA in mixed solvents (1.13 times more than that in pure THF solution) occurred at an f_w value of 70% (Fig. 1f). The twisted intramolecular charge transfer effect (TICT) of SOTA molecule was responsible for this enhanced fluorescence. To be underlined, the fluctuating fluorescence emission was proof to justify that SOTA was in the AIE family, which encouraged us to pave the way for its application in fluorescence imaging and photodynamic therapy.

Characterization of SOTA NPs

The synthesized SOTA and poly(ethylene oxide)–poly(propylene oxide)–poly(ethylene oxide) (PEO–PPO–PEO) (F127, Scheme 1), which behaved as the peripheral encapsulating polymer, were co-precipitated into nanoparticles (SOTA NPs) with a concentration of 278.3 μM (Fig. S8, ESI†). Both spectra of SOTA NPs in the nano-aggregated state in Fig. 1g resembled those in the THF solution (Fig. 1a), except for the typical redshift of 11 nm for the absorption spectrum and 15 nm for the fluorescence spectrum. It was evident that aggregation would account for this discrepancy and F127 had no influence on the intrinsic properties of SOTA NPs. Besides, SOTA NPs were equipped with an approximate size of 84.5 nm (Fig. 1h), spherical morphology, as well as satisfied long-term stability, as proved by the small fluctuation of the mean sizes between 84–89 nm for SOTA NPs dispersed in water in a period of 15 days (Fig. 1i). This conclusion was supported by the average sizes in the range of 84–93 nm in four different media (ultrapure water, 10% FBS in PBS, PBS, and DMEM) (Fig. S9, ESI†). Moreover, its Zeta potential of −15.31 mV was smaller as compared to SOTA (−21.87 mV) (Fig. S10, ESI†).

Because of intense intramolecular charge transfer (ICT) from the TPA donor to the SO receptor, it is hypothesized that SOTA exhibits favourable two-photon absorption properties. To

accurately quantify the two-photon absorption (2PA) behaviour of SOTA NPs, we employed the two-photon excited fluorescence (2PEF) technique with a femtosecond (780 nm) Ti–sapphire laser source to identify the 2PA cross sections (δ) in the 700–900 nm range (Fig. S11, ESI†). It was gratifying to conclude that the SOTA NPs exhibited bright green emission and impressive 2PA signatures across the 700–940 nm wavelength range in the NIR-I region. The δ_{max} of 7247 GM was achieved for SOTA NPs at 700 nm. It was worth mentioning that this excitation wavelength (700 nm) was about double the maximal absorption peak (360 nm), which conformed to the 2PA principle. Of note, we were motivated by the outstanding fluorescence quantum yield and 2PA capability in the NIR region of SOTA to pursue its prospects in bio-imaging.

Two-photon fluorescence image

Two-photon excitation (TPE) confocal microscopy was known to suffer fewer optical impairments and penetrate deeper than conventional one-photon excitation imaging, which was the reason why it was more appealing for *in vivo* imaging. We sequentially administered two-photon fluorescence imaging to the peritoneum and bladder. As seen in Fig. 2a and d, SOTA NPs enabled blood vessels to be explicitly labeled. In addition to large vessels ($\approx$0.58 mm), bladder capillaries with a diameter of $\approx$0.21 mm and an ultrahigh SNR value of 46.5 were also viewed effortlessly by two-photon fluorescence without the use of other instruments (Fig. 2b). At a penetration depth of 60 μm, full-width-at-half-maximum (FWHM) of the collected image was 5.57 μm with high SNR value of 15.2 (Fig. 2e). Likewise, the capillary structure of penetration could be determined. The depth of penetration was 295 μm for the bladder and 258 μm for the peritoneum from 3D images, respectively (Fig. 2c and f), which was elusive for one-photon excitation imaging.

Since the metabolic function of the liver, we additionally scanned the *ex vivo* liver tissue with 2P FL image after 2 h of SOTA NPs injection. It also acquired favorable fluorescence pictures in depths of 363 μm (Fig. 2g and i). Unlike the image at a depth of 50 μm, where the SNR value was not sufficient (Fig. S12, ESI†), it was raised to 14.6 when scan depth was set to 100 μm (Fig. 2h). This progressively better quality of pictures exemplifies the distinguished advantages of two-photon fluorescence imaging, namely penetration depth and signal-to-noise ratio.

ROS generation ability

Since SO-based polymers could behave as efficient photosensitizers,[28,29] we went on to explore the photodynamic properties of SOTA NPs. The photosensitizer underwent intersystem crossing during the photodynamic process, which was more prone to allow the preferential generation of $^1O_2$ from oxygen through energy transfer. Along with this guideline, we conducted an assessment if $^1O_2$ was generated by SOTA NPs as expected by the use of 9,10-anthracenediyl-bis(methylene) dimalonic acid (ABDA) as the indicator. ABDA reacted with $^1O_2$ continuously and caused its absorbance to attenuate. As indicated in Fig. 3a, an absorbance decreases of 53.8% for ABDA (50 μM) at 399 nm was evidenced after 5 min of white light exposure (100 mW cm^{-2}) with 10 μM SOTA NPs (Fig. 3b). That was to say, 26.9 nmol of ABDA was consumed by $^1O_2$ that was produced by 10 nmol SOTA NPs under 300 s irradiation of white light. SOTA NPs had a comparable capacity to produce $^1O_2$ as Methylene blue (MB), a well-known commercial photosensitizer. On the other hand, there was almost no decrement in the absorbance of ABDA without SOTA NPs (Fig. S13, ESI†). The significant differences in absorption intensity confirmed

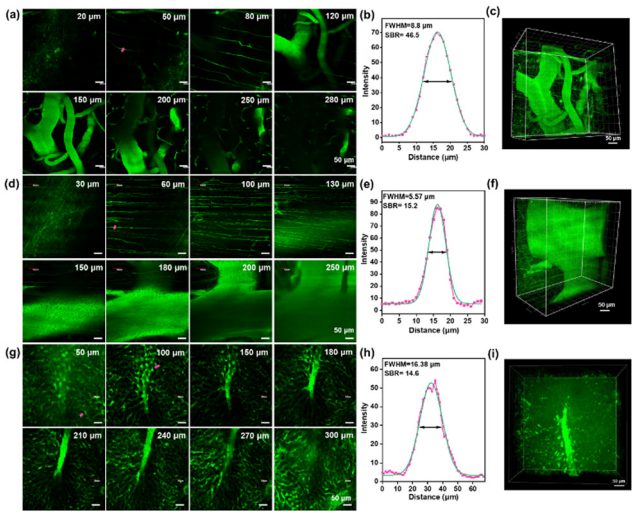

Fig. 2 Confocal fluorescent images of mouse organ vessels with SOTA NPs at different depths as indicated under excitation of two-photon laser (λ_{ex} = 700 nm), plots of pixel intensity across the capillaries (marked with a pink line) and 3D reorganization image: (a)–(c) bladder; (d)–(f) peritoneum; (g)–(i) liver, respectively. Scale bars: 50 μm.

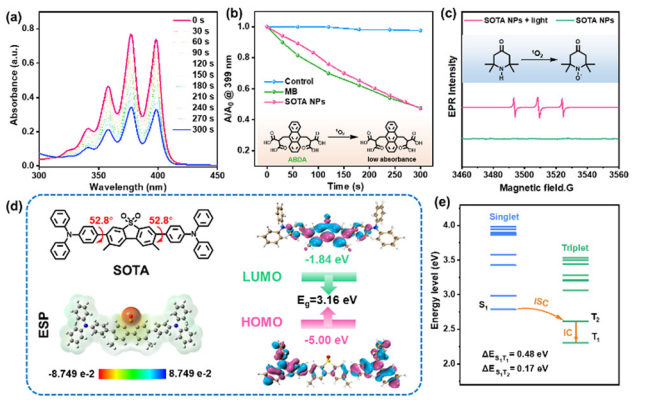

Fig. 3 (a) Time-dependent UV-vis absorption spectra of ABDA + SOTA NPs during white light irradiation. (b) Decomposition rate curves of ABDA by $^1O_2$ produced by SOTA NPs, MB, and the control pure water under white light irradiation. Here, A_0 and A represent the absorbance at 399 nm before and after irradiation, respectively. (c) EPR spectra of SOTA NPs by using TEMP in water as the capture agent. (d) Electrostatic potential map, HOMO–LUMO distribution, and ΔE_{gap} of SOTA (e) energy levels (S_1–S_{10}, T_1–T_{10}) of SOTA calculated by the vertical excitation of the optimized structures. IC: internal conversion.

that $^1O_2$ was generated as predicted, which was again unraveled with electron paramagnetic resonance (EPR) spectroscopy, using TEMP (2,2,6,6-tetramethylpiperidine) as O_2 indicator in Fig. 3c. A resonance of the TEMP/$^1O_2$ adduct (4-oxo-TEMPO),[30] harboring a 1 : 1 : 1 triplet signal was picked up by EPR spectroscopy during 5 min of xenon lamp illumination, which was the powerful signature that $^1O_2$ formed by SOTA NPs was trapped by probe TEMP (Fig. 3c). Furthermore, the photosensitization behavior of SOTA NPs was then evaluated by $^1O_2$ quantum yield (Φ_Δ) with MB (52%) as a reference.[31] As calculated from Fig. S14 (ESI†), such a decent Φ_Δ value of 58.5% motivated us to further explore its photodynamic therapy against cancer cells. Besides, the virtually identical absorption spectra of SOTA NPs before and after illumination in Fig. S15 (ESI†) were a convincing demonstration that SOTA resisted photo-bleaching, which was absent for the famous photosensitizer Ce6 (Fig. S16, ESI†).[32]

To clarify whether the design strategy of this AIE fluorophore was practicable or not, a density functional theory (DFT) calculation was conducted. In the electronic static potential (ESP) map, the sulfone group showed a negative value due to its strong electron-withdrawing nature. The electrostatic action of this polarizing sulfone group contributed to the tight packing of neighboring molecules, making the thermodynamic energy of SOTA stable.[33] Twist D–A–D conformation with dihedral angles of 52.8° for SOTA was revealed from its optimized ground-state molecular geometry (Fig. 3d), which likely was a factor in promoting the formation of a TICT state. It was also noticed that this torsional architecture boosted its solubility.[34]

The electron clouds of the HOMOs were concentrated on donor TPA unit and slightly dispersed to SO core, while the LUMOs were predominantly dominated by acceptor SO unit (Fig. 3d). Consequently, the energy gaps of singlet and triplet were 0.48 eV for $\Delta E_{S_1-T_1}$ value and 0.17 eV for $\Delta E_{S_1-T_2}$ value (Fig. 3e). ISC happened between S_1 and T_2, and then the internal conversion from T_2 to T_1 would occur. Hence, this pathway increased the probability of ISC, which may be an explanation for a favorable $^1O_2$ yield of 58.5% for SOTA NPs.

In vitro PDT

In view of the decent sensitization ability of SOTA NPs, we have thoroughly characterized the *in vitro* photodynamic therapeutic ability of SOTA NPs by justifying the decreased magnitude in absorbance of ABDA. Endocytosis of the foreign nanoparticles by cells was fundamental for the implementation of photodynamic therapy at the cellular level. Prior to the photodynamic experiments, 4T1 and A549 cells were pre-cultured with SOTA NPs for four time points at two-hour intervals (2, 4, 6, and 8 h). As the duration of incubation was prolonged to 8 h, the accumulation of SOTA NPs in the cytoplasm was maximized at 6 h (Fig. 4a and b), as judged by a notable amplification followed by a slight diminution of the green signals from SOTA NPs. The trend of fluorescence change in A549 cells was consistent with that in 4T1 cells, but the signal intensity was generally preferable to that in 4T1 cells (Fig. S17, ESI†). Therefore, we ascertained A549 cells for subsequent experiments for the sake of ensuring a good therapeutic effect.

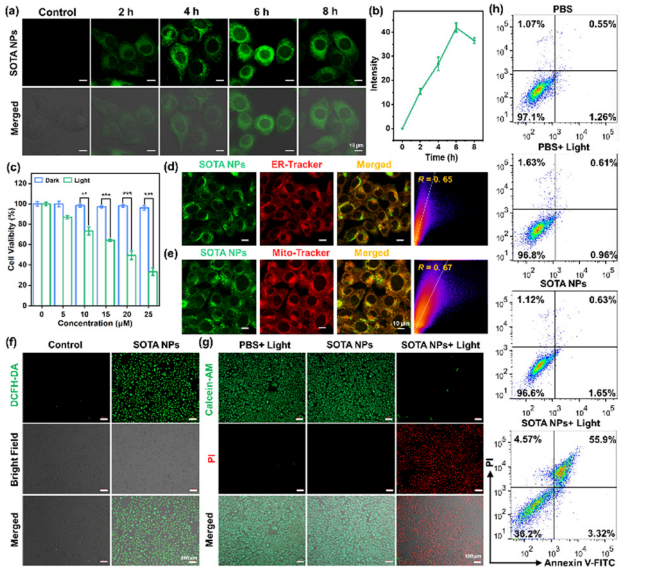

Fig. 4 (a) Cellular uptake and (b) fluorescence intensities of A549 cells after co-incubation of SOTA NPs (15 μM) at time points of 0, 2, 4, 6, 8 h. Scale bars: 10 μm. (c) Dark cytotoxicity and light cytotoxicity test in A549 cells of the AIE photosensitizer SOTA NPs (400–780 nm, 100 mW cm^{-2}, 5 minutes). Data are represented as mean ± SD (n = 5). Statistical p-values: $^{**}p < 0.01$, $^{***}p < 0.001$. Confocal fluorescence images of AIE photosensitizer SOTA NPs co-localization of (d) endoplasmic reticulum and (e) mitochondria in A549 cells. Scale bars: 10 μm. (f) ROS fluorescence imaging of the AIE photosensitizer SOTA NPs in A549 cells. Scale bars: 100 μm. (g) Live/dead cell staining images after different treatments. Scale bars: 100 μm. (h) Apoptosis assay of A549 cells after various treatments (PBS, PBS + light, SOTA NPs, SOTA NPs + light). The concentration of SOTA NPs was 25 μM.

Next, biocompatibility and photodynamic effect of SOTA NPs in the presence of white light administration on A549 cells were checked by Cell Counting Kit-8 (CCK-8) method, respectively (Fig. 4c). The biosafety of SOTA NPs was demonstrated by the fact that more than 90% of cells survived at concentrations ranging from 0 to 25 μM. SOTA NPs were stimulated by light for a duration of 5 min and generated abundant toxic $^1O_2$, rendering cell death to achieve the expected therapeutic effect with a concentration-dependent mortality rate. At the nanoparticle concentration of 25 μM, the percentage of A549 cell survival plummeted from 96% in the absence of white light to 33% in the presence of white light. This 2.9-fold magnitude of decrease was reflective of the exceptional phototoxicity of SOTA NPs.

The distribution of nanoparticles in organelles was directly associated with phototherapeutic performance, and mitochondria and endoplasmic reticulum were described to account for the apoptosis of tumor cells.[35,36] Thus, co-localization experiments were undertaken with the designated probes to shed tentative light on the death initiation of A549 cells. The overlapping confocal laser scanning microscopy (CLSM) image showed bright yellow fluorescence signal from green fluorescence of SOTA NPs and red fluorescence of two probes. The successful targeting of SOTA NPs to either endoplasmic reticulum or mitochondria was mainly manifested by Pearson's correlation coefficient of 65% for endoplasmic reticulum and

67% for mitochondria in Fig. 4d and e. Such efficient targeting function of SOTA NPs was beneficial for the ablation of cancer cells during photodynamic therapy.

Dichlorodihydrofluorescein diacetate (DCFH-DA) was oxidized intracellularly with reactive oxygen species to obtain DCF, along with fluorescence being switched on to green fluorescence. This characteristic was capitalized on to study the potential of SOTA NPs to induce intracellular generation of ROS. A549 cells were separately co-cultured with PBS as the control group and SOTA NPs as the experimental group under white light stimulation for 6 h. Then two groups were imaged by CLSM to identify whether ROS were generated. Definite green fluorescence emitted by DCF appeared in the latter, as opposed to the former control group, which was devoid of noticeable fluorescent signals (Fig. 4f). This marked comparison gave insight into the fact that SOTA NPs were the promising photosensitizer to produce $^1O_2$. As a convenient and straightforward observation of photodynamic therapeutic results of SOTA NPs, we affirmed the positive conclusion again by conducting the live/dead cell (calcein-AM/PI) double staining experiments against A549 cells using CLSM. An absence of cell death after being subjected to PBS and white light treatment or SOTA NPs treatment alone was observed in Fig. 4g, indicative of the safety of the light source and SOTA NPs utilized in the PDT experiment. On the contrary, a combination of SOTA NPs and white light induced most of the A549 cell death, as witnessed by the emergence of red fluorescence in Fig. 4g, further indicating that the SOTA NPs have great potential for application as an efficient photosensitizer for PDT. The flow cytometry analysis was performed to comprehensively investigate the apoptosis of A549 cells treated by PDT (Fig. 4h). In agreement with the control groups (PBS group and PBS + light group), the percentage of viable A549 cells in the SOTA NPs group was 96.6%, demonstrating its minimal toxicity and excellent biocompatibility. In the case of the SOTA NPs + light group, it exhibited profound A549 cell apoptosis with a high apoptotic percentage of 55.9%. These findings matched well with that of CCK-8 results, again emphasizing the fact that SOTA NPs were one promising candidate for PDT against cancer cells with light toxicity, instead of dark toxicity.

Conclusions

In conclusion, an AIE-active photosensitizer (SOTA) with near-infrared light excitation and high $^1O_2$ generation efficiency was designed for *ex vivo* two-photon fluorescence imaging and photodynamic therapy. Although the absorption of SOTA was in the visible region, it was excited by long-wavelength visible light at a wavelength of 700 nm to emit bright green fluorescence. The two-photon fluorescent contrast agent AIEgen achieved a moderate penetration depth of 295 μm and an ultra-high SNR value of 46 in fluorescence imaging *in vivo*. Upon illumination with white light, SOTA performed better than the widely used commercial photosensitizer MB in generating $^1O_2$, due to highly efficient intersystem crossing process. The SOTA nanoparticles displayed superior photodynamic potential in both aqueous media and cells, inducing apoptosis in 67% of A549 cells. Altogether, it opened new avenues for the development of multifunctional AIE fluorophores for two-photon fluorescence imaging and photodynamic therapy.

Author contributions

L. W. Hu conceived the concept of developing the AIE-active photosensitizer and supervised the project. T. Z. Hu contributed to experimental design and performed the experiments. C. X. Wang guided the experiments. T. Guo wrote and checked the manuscript.

Data availability

The data supporting this article have been included as part of the ESI.†

Conflicts of interest

There are no conflicts to declare.

Acknowledgements

The authors are grateful for the financial support from National Natural Science Foundation of China (22205081), Knowledge Innovation Program of Wuhan-Shuguang Project (2023010201020449).

Notes and references

1 D. Ding and B. Z. Tang, *Adv. Healthcare Mater.*, 2021, **10**, 2102499.
2 Y. Q. Zhou, X. F. Yang, X. Z. Wei, S. S. Zhang and M. Yan, *Coord. Chem. Rev.*, 2024, **513**, 215864.
3 T. Etrych, H. Lucas, O. Janoušková, P. Chytil, T. Mueller and K. Mäder, *J. Controlled Release*, 2016, **226**, 168.
4 S. H. Roy, N. Bag, S. Bardhan, I. Hasan and B. Guo, *Adv. Drug Delivery Rev.*, 2023, **197**, 114821.
5 D. D. Chen, T. Xiao, L. J. Wang, S. J. Chen, C. Kam and G. P. Zeng, *Aggregate*, 2024, e550.
6 Z. Li, P. Z. Liang, L. Xu, X. X. Zhang, K. Li and Q. Wu, *Nat. Commun.*, 2023, **14**, 1843.
7 B. Guo, Z. Feng, D. H. Hu, S. D. Xu, E. Middha and Y. T. Pan, *Adv. Mater.*, 2019, **31**, 1902504.
8 B. Wang, H. Zhou, L. Chen, Y. C. Ding, X. Y. Zhang and H. Y. Chen, *Angew. Chem., Int. Ed.*, 2023, **63**, e202408874.
9 M. Cheng, Q. J. Kong, Q. Tian, W. L. Cai, C. M. Wang and M. J. Yuan, *J. Nanobiotechnol.*, 2024, **22**, 151.
10 Q. L. Yang, H. L. Ma, Y. Y. Liang and H. J. Dai, *Acc Mater. Res.*, 2021, **2**, 170.
11 C. B. Li, J. Du, G. Y. Jiang, J. Y. Gong, Y. Zhang and M. F. Yao, *Nat. Commun.*, 2024, **15**, 5832.
12 Q. S. Zhang, P. Yu, Y. Fan, C. X. Sun, H. S. He and X. Liu, *Angew. Chem., Int. Ed.*, 2021, **60**, 3967.
13 Y. Jiang, Y. G. Zhang, Y. F. Deng, S. Q. Dong, B. Li and Y. P. Yi, *CCS Chem.*, 2022, **4**, 3497.

14 J. Qi, X. C. Duan, W. Y. Liu, Y. Li, Y. J. Cai and J. W. Y. Lam, *Biomaterials*, 2020, **248**, 120036.
15 S. J. Liu, H. L. Ou, Y. Y. Li, H. K. Zhang, J. K. Liu and X. F. Lu, *J. Am. Chem. Soc.*, 2020, **142**, 15146.
16 H. R. Wang, Q. Y. Li, P. Alam, H. T. Bai, V. Bhalla and M. R. Bryce, *ACS Nano*, 2023, **17**, 14347.
17 Z. Wang, Y. Zhou, R. H. Xu, Y. Z. Xu, D. F. Dang and Q. F. Shen, *Coord. Chem. Rev.*, 2022, **451**, 214279.
18 Z. Li, B. Z. Tang and D. Wang, *Adv. Mater.*, 2024, e2406047.
19 J. F. Wang, M. Y. Cao, L. L. Han, P. S. Guan, Y. S. Liu and Y. Zhong, *J. Am. Chem. Soc.*, 2024, **146**, 28783.
20 S. X. Cao, X. Y. Tian, M. Y. Cao, J. G. Wang, G. L. Niu and B. Z. Tang, *Chem. Mater.*, 2023, **35**, 2472.
21 Y. W. Wang, J. H. Liao, Y. T. Lyu, Q. Q. Guo, Z. R. Zhu and X. P. Wu, *Adv. Funct. Mater.*, 2023, **33**, 2301692.
22 Y. Xu, D. S. Tang, L. J. Li, X. Li, Q. Chang and H. H. Xiao, *Adv. Funct. Mater.*, 2024, e2315385.
23 T. Hua, L. S. Zhan, N. Q. Li, Z. Y. Huang, X. S. Cao and Z. Q. Xiao, *Chem. Eng. J.*, 2021, **426**, 131169.
24 C. Y. Li, D. J. Liu, Y. J. Hong, R. F. Lin, Z. C. Liu and M. Chen, *Angew. Chem., Int. Ed.*, 2022, **1**, e202202005.
25 Z. Fan, K. X. Teng, Y. Y. Xu, L. Y. Niu and Q. Z. Yang, *Angew. Chem., Int. Ed.*, 2024, e202413595.
26 A. Soleimany, D. K. Aghmiouni, M. Amirikhah, M. A. Shokrgozar, S. Khoee and B. Sarmento, *Adv. Funct. Mater.*, 2024, **34**, 2408594.
27 Q. Q. Yu, J. W. Li, Y. L. Yu, M. M. Yan, D. D. Xu and S. C. Yin, *Coord. Chem. Rev.*, 2024, **518**, 216056.
28 L. W. Hu, Z. K. Chen, Y. S. Liu, B. S. Tian, T. Guo and R. Y. Liu, *ACS Appl. Mater. Interfaces*, 2020, **12**, 57281.
29 L. W. Hu, L. R. Shi, T. Z. Hu, C. Liu, T. Guo and C. X. Wang, *Ind. Eng. Chem. Res.*, 2024, **63**, 1748.
30 B. Wang, W. L. Wang, K. Sun, Y. J. Xu, Y. Sun and Q. Li, *Nano Res.*, 2023, **16**, 11992.
31 Y. F. Xiao, W. C. Chen, J. X. Chen, G. H. Lu, S. Tian and X. Cui, *ACS Appl. Mater. Interfaces*, 2022, **14**, 5112.
32 W. B. Wu, D. Mao, S. D. Xu, Kenry, F. Hu and X. Q. Li, *Chemistry*, 2018, **4**, 1937.
33 J. R. Yu, H. J. Tan, X. Q. Gao, B. Wang, Z. Q. Long and J. L. Liu, *Adv. Sci.*, 2024, **11**, 2401664.
34 C. Z. Zhu and L. Fang, *Macromol. Rapid Commun.*, 2018, **39**, 1700241.
35 Y. Yuan, Y. S. Ju, Y. W. Kim, J. Li, Y. M. Wang and C. J. Yoon, *Nat. Genet.*, 2020, **52**, 342.
36 W. Li, J. Yang, L. H. Luo, B. Qin and H. Yin, *Nat. Commun.*, 2019, **10**, 3349.